Detached Eddy Simulation of a Sailing Yacht

Ocean Engineering 90 (2014) 93–103

Contents lists available at ScienceDirect

Ocean Engineering

journal homepage: www.elsevier.com/locate/oceaneng

Detached Eddy Simulation of a sailing yacht

Ignazio Maria Viola [a,*], Simone Bartesaghi [b], Thomas Van-Renterghem [c], Raffaele Ponzini [d]

[a] Institute for Energy Systems, School of Engineering, The University of Edinburgh, Room 3.93, Faraday Building, The King's Buildings, Mayfield Road, Edinburgh EH9 3JL, UK
[b] Department of Mechanical Engineering, Politecnico di Milano, Italy
[c] A320 NEO Pylon Manufacturing Engineering, Airbus Operations SAS, Saint-Eloi, Toulouse, France
[d] SuperComputing Applications and Innovation Department, CINECA, Italy

ARTICLE INFO

Article history:
Received 20 November 2013
Accepted 30 July 2014
Available online 21 August 2014

Keywords:
Sailing yacht
Sail aerodynamics
Delayed Detached Eddy Simulation
DES
Leading edge vortex
Pressure distributions

ABSTRACT

Wind tunnel experiments on a 1:15th model-scale yacht were modelled with Detached Eddy Simulations, which allowed drawing the topology of the turbulent structures in the sail wake discovering new flow features. Simulations were performed with two different grids and three different time steps. It was found that a leading edge vortex grows from the foot to the head of the spinnaker (foresail), where it deflects downstream forming the tip vortex. The twist of the spinnaker leads to a mid-span helicoidal vortex, which has a horizontal axis almost parallel to the apparent wind and rotates in the same direction of the tip vortex. Vortical spanwise tubes are released from the trailing edge of the mainsail (aftsail) and the spinnaker and roll around the tip and the mid-span vortex of the spinnaker. Vortical tubes are also detached intermittently from the sails' feet and these break down into smaller and smaller structures while convecting downstream. For comparison, we also performed a Reynolds-averaged Navier–Stokes simulation. The comparison between forces and pressure distributions computed with different grids and time resolutions, different turbulence models, and measured with flexible and rigid sails showed similar trends; differences between numerical results were smaller than those between experimental results.

1. Introduction

Foresails are thin airfoils where the flow separates at the leading edge due to the sharpness of the edge and reattaches further downstream, leading to a high suction peak on the sail surface and contributing significantly to the overall thrust force. This flow feature is known as leading edge vortex (LEV) (Maxworthy, 2007) and it occurs on insect wings (Birch and Dickinson, 2001) and bird wings (Videler et al., 2004) at low Reynolds numbers (*Re*), and on delta wings at high *Re* (Gursul et al., 2007). The general features are also similar to those of the long laminar separation bubble known on thin airfoils with a sharp leading edge (Owen and Klanfer, 1953) but while the LEV is a coherent flow structure, the laminar separation bubble results from the time average of an unsteady flow field.

Downstream of the reattachment point, a boundary layer develops and the sail curvature leads to a second suction peak. Highly cambered sails show significant trailing edge separation due to the adverse pressure gradient downstream of this second suction peak. The sharp leading edge suction peak and the second smoother suction peak due to the sail curvature are typical of sails and unusual on airfoils. Fig. 1 shows the typical flow and pressure fields where a highly cambered spinnaker (foresail) and a flatter and smaller mainsail (aftsail) are used.

Differently from aircraft wings, sails are significantly twisted and cambered both chordwise and spanwise leading to a characteristic wake, which is not found on typical aeronautical wings. The flow field in the wake is measured with difficulty and experimentally while it can be computed numerically. The relatively high *Re* and the complex 3D geometry make direct numerical simulations unfeasible and therefore turbulence must be modelled. Reynolds-averaged Navier–Stokes simulations (RANS) have been performed since 1996 on downwind sails (Hedges et al., 1996) and, since then the agreement between numerical and experimental forces has increased in parallel with the growth of computational resources. The number of grid cells increased by about one order of magnitude every three years, Hedges et al. used a number of grid cells of the order 10^3, three years later Miyata and Lee (1999) used a number of grid cells of the order 10^4, and ten years later Viola (2009) used a number of grid cells of the order 10^7.

Richards and Lasher (2008) and Viola and Flay (2011) compared surface pressure distributions computed with RANS to those measured in wind tunnels. They found good agreement on the mid sections of the sails but larger differences on the highest sail

* Corresponding author. Tel.: +44 131 650 5622; fax: +44 131 650 6554.
E-mail address: i.m.viola@ed.ac.uk (I.M. Viola).

http://dx.doi.org/10.1016/j.oceaneng.2014.07.019
0029-8018/

sections, where the suction peak near the leading edge was under-predicted by RANS.

While RANS allows a reasonable estimate of the pressure distributions, it does not allow an in-depth understanding of the turbulent structures in the wake. Therefore we performed Detached Eddy Simulations (DES), where the turbulence is modelled with RANS in the boundary layer and Large Eddy Simulation in the wake. As far as known by the authors, the present paper presents the first published investigation on sail aerodynamics performed with DES. However, it must be noted that Braun and Imas (2008) stated that DES was used in the design process of an ACC-V5-class yacht for the 32nd America's Cup, though no results were presented; Wright et al. (2010) presented few results achieved with DES but no details were provided to verify the validity of the simulation. In the present paper, the wind tunnel test on a spinnaker with both RANS and DES, using different grids and time steps, are presented.

The paper is structured as follows: in Section 2, the experimental tests are introduced and the numerical simulations modelling the experiments are described, including details of the equations solved, the boundary conditions, the grids and the time steps tested, and the hardware used to run the simulations. In Section 3, the general flow field computed with the numerical simulations is presented, and details of the near-wall region and of the sail wake are discussed. Forces and pressures computed with the different simulations are compared with the experimental data. In Section 4, the key findings of the research are summarised.

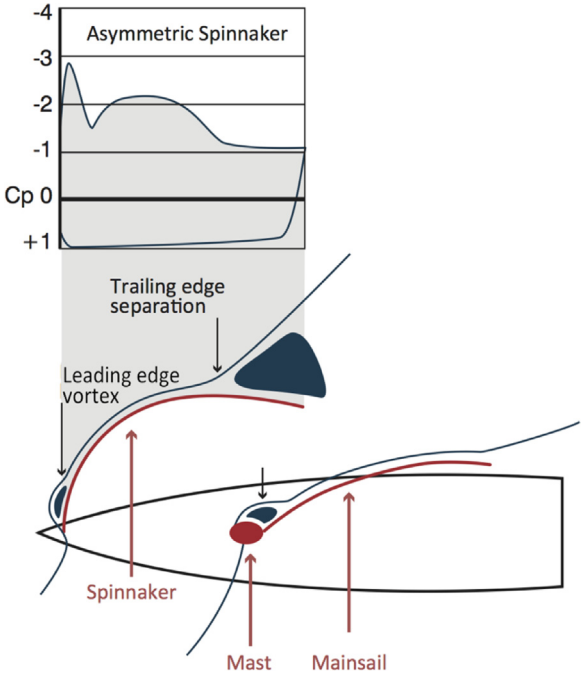

Fig. 1. Typical flow and pressure distributions in downwind conditions.

2. Method

2.1. Wind tunnel tests with flexible sails

A 1:15th model-scale AC33-class yacht equipped with flexible sails was tested at the Auckland University wind tunnel. Fig. 2 (left) shows the model during the wind tunnel test. The tunnel has a 3.5-m-high and 7-m-wide open jet section, where the floor and the roof extend downstream for 5.1 m and 4.8 m, respectively. The 2.3-m-high model was placed on the wind tunnel floor at 2.7 m downstream from the open jet section. A flexible spinnaker and a mainsail were mounted on a model scale yacht, which included the hull and the rigging, at 55° apparent wind angle and 10° heel angle. Viola and Flay reported the force (2009) and pressure (2010) measurements. The mean flow velocity was $U_\infty = 3.5$ m/s, equivalent to a dynamic pressure $q_\infty = 7.5$ Pa. The boundary layer on the

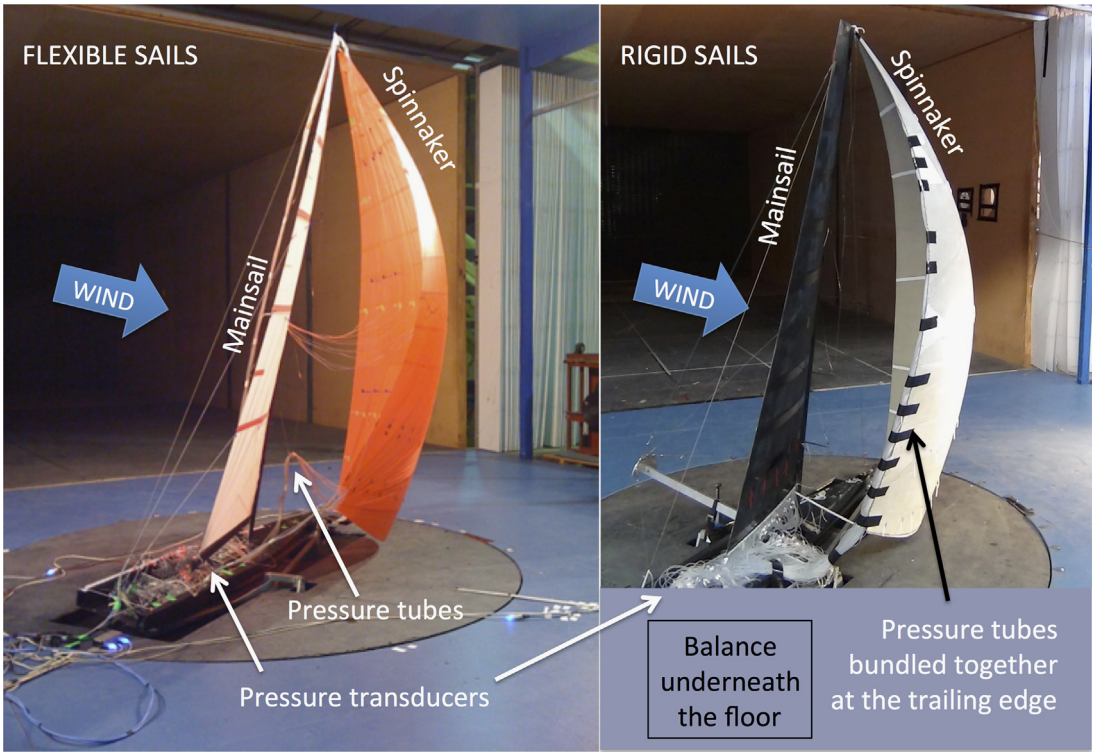

Fig. 2. Wind tunnel tests performed with flexible sails (left) and rigid sails (right).

floor was measured in the empty wind tunnel at the model location. The boundary layer height was 0.25 m and the velocity profile could be approximated by $u^+ = 1.9(y^+)^{0.16}$, where u^+ is the mean velocity normalised by the friction velocity and y^+ is the distance from the wall normalised by the viscous length scale. The turbulent intensity was $T_u = 0.03U_\infty$ outside of the boundary layer, and it increased almost linearly from $T_u = 0.07U_\infty$ at 0.2 m from the wall to $T_u = 0.12U_\infty$ at 0.005 m from the wall. The turbulent length scale, L_t, was not measured. Forces were measured using a 6-component balance placed underneath the wind tunnel floor, and sail surface pressures were measured using pressure taps attached to the sails. Pressure taps were 20-mm long, 10-mm wide and 4-mm height, attached to the sail on the opposite side to that under investigation, and a 1-mm-diameter hole was made in the sail to allow pressure transmission to the tap. PVC tubes with a 1-mm internal diameter, suspended from the sail to the boat mast, carried the pressures from the tap to the pressure transducers located on the boat deck. Pressure taps were placed on five horizontal sections at heights of 1/8, 1/4, 1/2, 3/4 and 7/8 of the mitre, which is the line on the sail surface equally far from the leech and the luff (leading and trailing edge, respectively). The far-field static pressure p_∞ was computed by the difference of the total and dynamic pressures measured by a Pitot static probe located approximately 10 m upstream at the top-mast height. The pressure transducers measured the difference between the sail surface pressure and p_∞ at 100 Hz. Pressure coefficients, C_p, were computed dividing this difference by the dynamic pressure, q_∞, which was time-averaged over a period of 70 s and was about 7.5 Pa. Forces were measured at 200 Hz and averaged over the same period of 70 s. Uncertainties in the measurement of C_p were estimated to be about $U_{C_p}^- = 0.2$ and $U_{C_p}^+ = 0.1$ for the leeward and windward sides, respectively. Several photographs were taken during the tests and were used to detect the flying shapes of the two flexible sails in order to make a mathematical model, which was used to perform numerical simulations and, successively, to build rigid sails for further tests.

2.2. Wind tunnel tests with rigid sails

The mathematical model of the flying shapes was used to build a CAD/CAM wooden mould, which, in turn, was used to build rigid sails with fibreglass and a sandwich structure (Bot et al., 2013). The sails were less than 4-mm thick, mainly due to the thickness of the core, with the external fibreglass layer of negligible thickness. The thickness/chord ratio was less than 1% and the leading edge was chamfered at 45° in order to achieve a sharp edge. The core was made of extruded polypropylene, resulting in parallel square tubes. These were used to carry the pressure from 1-mm-diameter holes on the sail surface to the trailing edge, where 1-mm internal-diameter PVC tubes, gathered together along the trailing edge towards the sail foot, carried the pressure to the pressure transducers located on the boat deck. Fig. 2 (right) shows the model during the wind tunnel tests. The same testing set-up as the one adopted with flexible sails was used; pressures were measured at the same sail sections, forces and pressures were measured with the same instrumentation, at the same frequency and averaged over 70 s. Uncertainties in the measurement of C_p were estimated to be the same as for flexible sails.

It will be showed in Sections 3.5 and 3.6 that significant differences were found between the forces and pressure distributions measured with flexible and rigid sails. Subsequent studies (Paillaud, 2013) highlighted the large uncertainty in the sail shapes both for the flexible sails, due to inaccuracies of the photogrammetric method, and for the rigid sails, due to the deformations experienced for their own weight being suspended only from the head and tack corners. Further work is in progress in order to enhance the experimental technique and to provide a more accurate benchmark for CFD.

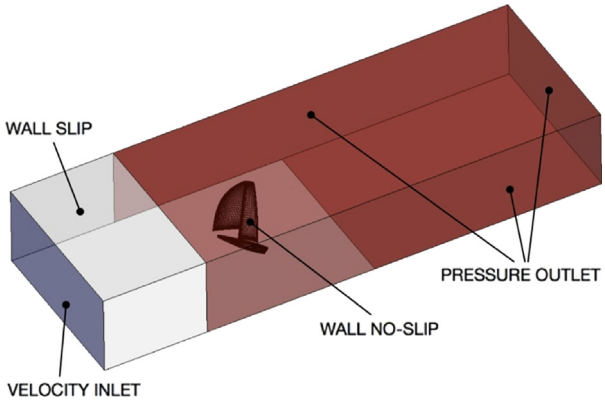

Fig. 3. Computational domain and boundary conditions.

2.3. Computational domain and boundary conditions

The detected flying shapes of the sails were used to perform the numerical simulations. Sails, mast, boom (horizontal mast at the mainsail foot) and hull were modelled with a non-slip condition. A prismatic computational domain 3-m high, 6.2-m wide and 18.4-m long was used to model the wind tunnel (Fig. 3).

The onset vertical velocity profile and the turbulence intensity profile measured in the wind tunnel experiment were used as inlet condition. The turbulent length scale was not measured and $L_t = 0.01$ m ($\approx h/200$) was used. It should be noted that L_t could have been under-estimated by about one order of magnitude and care is recommended for the choice of this parameter in future research. Non-slip condition was used on the floor boundary, which extend 3.5 m downstream from the model. The wind tunnel sidewalls and roof were modelled with slip-conditions but the computational domain extended downstream further than the end of the physical roof and floor, therefore pressure outlet conditions were used on these boundaries (Fig. 3).

2.4. Grids

Two non-structured hexahedra grids were built with Pointwise version 16.04 R1. The coarse grid was made of four million cells (4M). Fig. 4 shows the surface grid on the spinnaker (left) and a grid section at 1/2 of the spinnaker's mitre height (right). The 4M grid allowed modelling the spinnaker with about 60 cells chord-wise and about 64 cells spanwise. A finer grid was achieved using the hanging node function of Ansys Fluent version 13.0.0, which split every cell in eight cells leading to a 32-million-cells grid (32M). Table 1 shows the maximum and minimum y^+ computed by different simulations on the suction side of the spinnaker.

2.5. Reynolds-averaged Navier–Stokes

The incompressible steady RANS equations for Newtonian fluids were solved with the finite-volume pressure-based solver of Ansys Fluent version 13.0.0. The Spalart–Allmaras turbulence model with a vorticity-based production term was preferred to more accurate two-equations models in order to decrease the computational time. The production term of the modified turbulent viscosity $\tilde{\nu}$ was computed with a vorticity-based approach, and at the inlet it was set as follows: $\tilde{\nu} = 3^{0.5}2^{-0.5}U_\infty T_u L_t$. A SIMPLEC scheme was used to couple velocity and pressure. A second-order-accurate centred discretisation algorithm was used

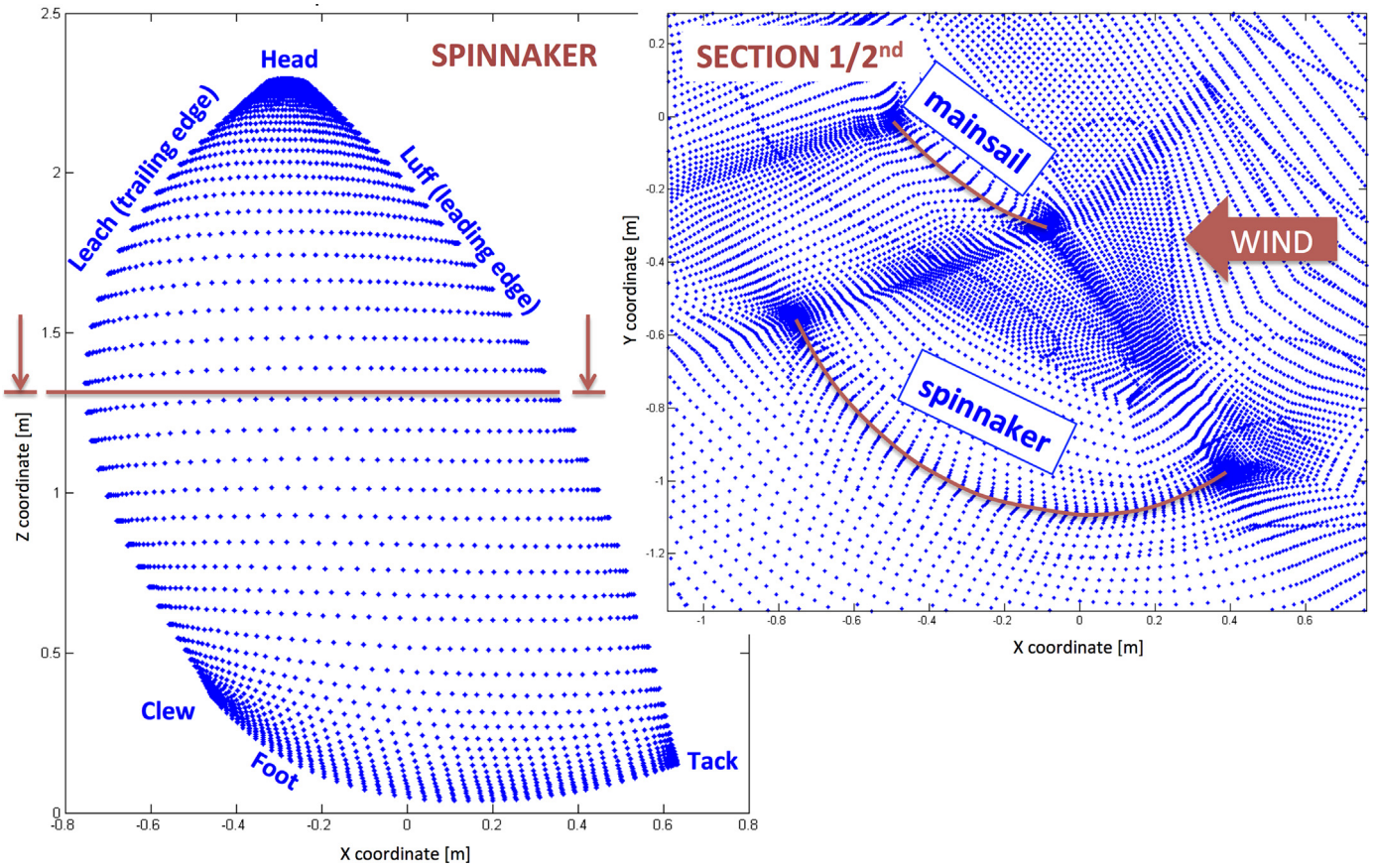

Fig. 4. Side view of the spinnaker's grid and plan view on a section at the spinnaker's mid height.

Table 1
y^+ for the two grids computed with RANS and DES.

	Min	Max
4M RANS	0.58	8.56
4M DES	0.76	9.05
32M DES	0.19	5.54

for the pressure, while second-order-accurate upwind algorithms were used for momentum and modified turbulent viscosity.

2.6. Detached Eddy Simulation

The transient Navier–Stokes equations were solved with a DES approach. The Spalart–Allmaras turbulence model was used to model the turbulence in the RANS region. In order to preserve the RANS model throughout the whole boundary layer, the DES length scale was modified as suggested by Spalart et al. (2006) for the Delayed Detached Eddy Simulation approach. A SIMPLEC scheme was used to couple velocity and pressure. The second order accuracy discretisation algorithm was used for the pressure, while second order central difference algorithms were used for momentum and modified turbulent viscosity. The fluctuating velocity components at the inlet were computed by synthesising a divergence-free velocity-vector field from the summation of randomly generated 100 Fourier harmonics using the method proposed by Smirnov et al. (2001). The resulting time-dependent flow field has the prescribed turbulent intensity and length scale but it does not model coherent flow structures, which will be generated in a region downstream of the boundary. Smirnov et al. argued that if the synthetic flow field is generated from realistic turbulence quantities and spectra then this region will be small. However, interested readers can consult a comparative study on different inlet conditions for LES by Tabor and Baba-Ahmadi (2010).

Table 2
Test matrix of the numerical simulations.

Method	Space Discretisation	Time Discretisation
RANS	4M grid	Steady
DES	4M grid	0.0005 s
DES	4M grid	0.0010 s
DES	4M grid	0.0020 s
DES	32M grid	0.0010 s

2.7. Test matrix

A RANS simulation was performed on the 4M grid, while DES simulations were performed on both the 4M grid and the 32M grid. On the coarser grid, time steps of 0.001 s, 0.002 s and 0.0005 s were used in order to estimate the uncertainty due to the time discretisation, while the maximum number of iterations per time step was kept constant to 20, allowing convergence at each time step. All these time steps allowed the Courant numbers in the sails' wake lower than one. For instance, with a time step of 0.001 s and the 4M grid, the Courant number ranged from 10^{-5} to 10^{-2}. On the 32M grid, only the intermediate time step (0.001 s) was used with 20 iterations per time step. Table 2 summarises the numerical simulations performed.

All the numerical simulations ran until convergence was achieved for the aerodynamic forces. In particular, lift, drag and heeling moment were monitored. Forces, pressure and velocity

fields computed with DES were averaged over a period of 10 s. For example, Fig. 5 shows the convergence of the drag coefficient C_d of the two sails (hull and rigging excluded) for the DES simulations performed with high grid resolution.

2.8. Hardware

All simulations were performed in double precision on a 64-bit Hewlett-Packard Linux cluster made of 336 nodes HP 2x220 2xIntel Exa-cores 3.166 GHz – 24 Gb RAM per node interconnected with Infiniband QDR and a node HP DL980 8 CPU Intel E5420 – 512 Gb RAM for post-processing and results visualisation. In order to take advantage of the High Performance Computing system, a preliminary scalability test using the smallest grid was performed. According to the scalability results the calculations on the different grid sizes have been performed using up to 256 computational cores. The 32M DES simulations converged after about 5 flow loops with a wall-clock time of 58 h/loop. Statistical data were gathered from the 6th and 7th loops.

2.9. Error bars

DES does not necessarily show asymptotic convergence with increasing resolution (Spalart, 2009) and therefore it is not possible to perform a formal verification and validation of the simulations. However the differences between time-averaged quantities computed with different time steps and grids provide a qualitative indication of the level of confidence in the numerical results. It is reasonable to expect that the uncertainty at, say 95% confidence level, is larger than the maximum differences computed with different time steps and grids by a multiplicative factor greater than one. Also, it can be assumed that the overall uncertainty is a combination of the uncertainty due to the time step and the grid. It was arbitrary decided to use a multiplicative factor of two and three for the uncertainty due to the time step and the grid, respectively, and to compute the overall uncertainty as the L2-norm of these two uncertainties. In Section 3.6, error bars are used to show the uncertainty so computed for the pressure coefficients. Due to the arbitrariness of this procedure, error bars should not be used as an exact measure of the uncertainty, but as a visual help to identify those regions where large differences in the results lead to a lower confidence in the results.

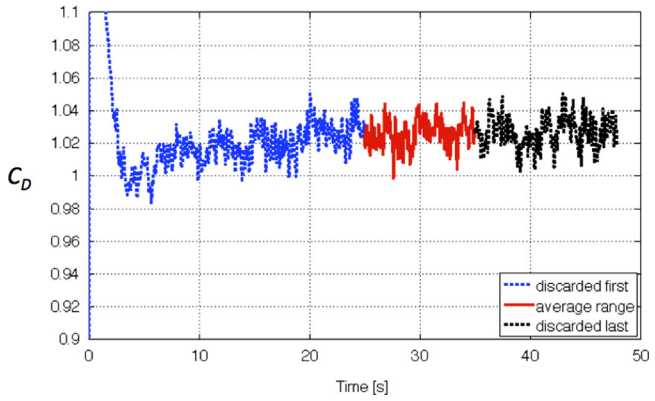

Fig. 5. Convergence of C_D for the DES 32M simulation.

Indeed the chosen multiplication factors, two for the time step uncertainty and three for the grid uncertainty, and the use of the L2-norm to combine the uncertainties are in agreement with the verification and validation guidelines for RANS simulations developed by Viola et al. (2013). In fact, the uncertainty $U_{t_{C_p}}$ due to the time step for the C_p was estimated using the following equation:

$$U_{t_{C_p}} = 1.5\,\frac{C_{p_{MAX}} - C_{p_{MIN}}}{1-(ts_{MIN}/ts_{MAX})} \tag{1}$$

where $C_{p_{MAX}}$ and $C_{p_{MIN}}$ are the maximum and the minimum time-averaged C_p, respectively, between those computed with time steps between $ts_{MIN} = 0.0005$ s, and $ts_{MAX} = 0.002$ s; while the uncertainty $U_{g_{C_p}}$ due to the grid for the C_p was estimated using the following equation:

$$U_{g_{C_p}} = 1.5\,\frac{C'_{p_{MAX}} - C'_{p_{MIN}}}{1-(\Delta_{MIN}/\Delta_{MAX})} \tag{2}$$

where $C'_{p_{MAX}}$ and $C'_{p_{MIN}}$ are the maximum and the minimum tim-averaged C_p, respectively, between those computed with an averaged node distance between $\Delta_{MIN} = (32\text{M})^{-1/3}$ and $\Delta_{MAX} = (4\text{M})^{-1/3}$.

3. Results

In the next sub-sections, firstly we provide an overview of the general flow field, then we show where the flow separates and reattaches along the spinnaker surface, including a description of the LEV, and then we discuss the different flow structures in the sail wake. Successively we discuss similarities and differences between forces and pressure distributions computed achieved with different numerical and experimental methods.

3.1. General flow field

Fig. 6 shows the general flow field around the yacht computed with RANS using the 4M grid. Pathlines are coloured by flow velocity. The grey scale shows the distributions of pressure difference between the pressure and the suction side of the sail. The larger delta pressures on the spinnaker than on the mainsail are due to the favourable upwash of the mainsail on the spinnaker,

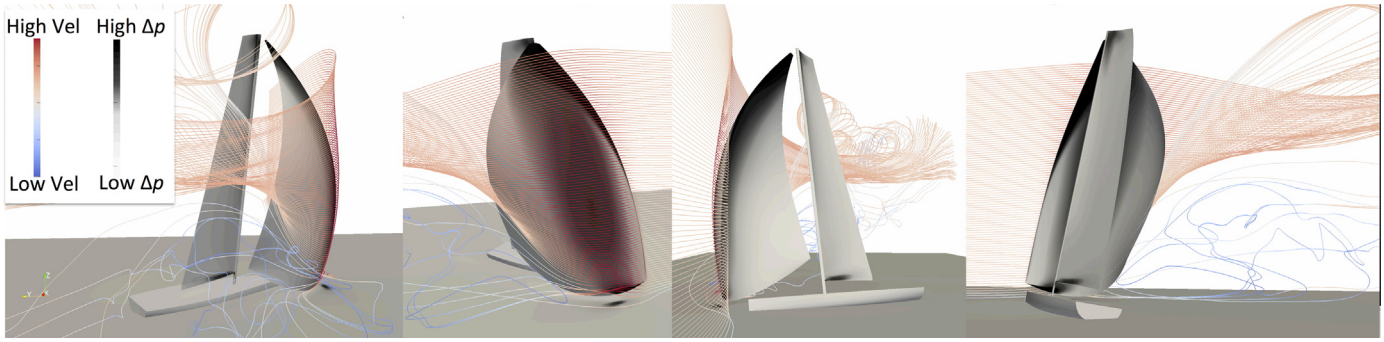

Fig. 6. Pathlines computed with RANS on the 4M-cell grid. (For interpretation of the references to colour in this figure, the reader is referred to the web version of this article.)

while the mainsail experiences the unfavourable downwash of the spinnaker.

On the leeward (suction) side of the spinnaker, the flow separates at the leading edge and reattaches downstream forming the leading edge vortex. The reattached boundary layer then separates near the trailing edge. Streamlines from the leading edge converge towards two vortical structures: the tip vortex at the head of the sails (not visible in Fig. 6) and a parallel vortex at mid-span height. As far as is known by the present authors, a *coherent and stationary* leading edge vortex and the mid-span vortex, which will be discussed in Sections 3.2 and 3.4, respectively, have never been identified before on a yacht sail.

On the windward (pressure) side, the flow is attached and the streamlines, which are not shown in Fig. 6, are slightly deflected upwards. This is due to the trailing edge being somewhat higher than the leading edge. In fact, the lower corner of the trailing edge (Fig. 4) is higher than the lower corner of the leading edge. Only those streamlines near the sail foot are attracted by the suction on the leeward side and are thus deflected downward convecting into the separated flow region downstream of the sail foot.

3.2. Leading edge vortex

Fig. 7 shows the flow field on the leeward surface of the spinnaker computed with the 4M-grid RANS (left), the 4M-grid DES (centre), and the 32M-grid DES (right). The same time step of 0.001 s is used for each of these simulations. For the DES simulations, red lines show the time-averaged flow field while white lines show the instantaneous flow field at 30 s. Red dash-dotted and red dotted lines are used to show time-averaged separation and reattachment lines, respectively. As a reference, several fractions of the spinnaker mitre are shown on the right-end side.

All simulations are able to model the flow separations at the sharp leading edge forming the LEV, which results continuous from the foot to the head of the sail. In particular, it is smaller near the foot and becomes progressively larger towards the head. The increase of vortex size generates a spanwise pressure gradient, which, in turns, leads to a high velocity field in the vortex core. The vorticity generated at the leading edge is convected towards the tip vortex by the spanwise velocity inside of the vortex core. The spanwise velocity is roughly 80% of the reference far field velocity, leading to a spanwise shear stress on the sail in correspondence of the vortex core as high as 3% of the dynamic pressure, i.e. twice as much as the maximum chordwise shear stress on the sail where the flow is attached. The LEV does not only generate a significant upward shear force, but it is also an exceptional lift generator. In fact, the high-speed swirling flow leads to a high suction.

3.3. Trailing edge separation

Trailing edge separation occurs somewhere on the second half of the chord (Fig. 7). Between 1/2 and 3/4 of the mitre, the flow is mostly horizontal before trailing edge separation occurs. Conversely, below 1/2 of the mitre, the attached boundary layer is deflected upwards. The upward deflection is more pronounced in the viscous sub-layer than in the logarithmic region. In fact, downstream of the reattachment point, the flow experiences a chordwise adverse pressure gradient, which slows to down, and a spanwise pressure gradient, which accelerates to upwards. In the boundary layer, these forces are equally applied to each layer, which therefore experiences the same acceleration. Over the same length, as opposed to the same time, the slowest layers will experience a higher deflection than the fastest layers.

In the separated region downstream of the trailing edge separation, the flow from the lower region moves upwards and converges towards the trailing edge separation line (dash-dotted line) between 1/2 and 3/4 of the mitre. Near the sail foot, the flow from the leading edge is deflected downwards driven by the shear layer stresses of the flow coming from the windward side and rolling over the sail foot.

The flow field near the spinnaker's clew is computed differently with low and high grid resolution. Only DES with high grid resolution predicts a clear trailing-edge separation from the sail foot to 3/4 of the mitre, while RANS and DES computed with low grid resolution do not show a continuous trailing-edge separation line.

The red lines in Fig. 7 (right) for the 32M-DES are in good agreement with the visual observations performed in the wind tunnel with rigid sails. In particular, the position of separation and

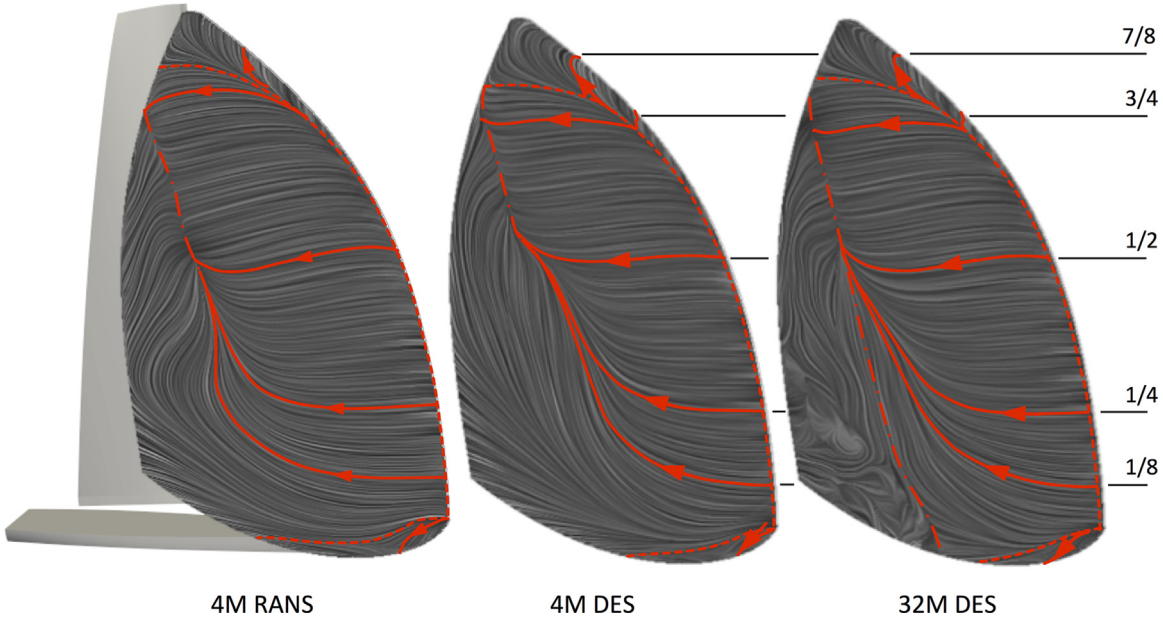

Fig. 7. Skin friction lines on the leeward side of the spinnaker computed by RANS and DES with the 4M-cell and the 32M-cell grids. (For interpretation of the references to colour in this figure legend, the reader is referred to the web version of this article.)

reattachment lines was qualitatively confirmed using a stick with a yarn tuft, while the upwards deflection in the attached flow region was found less pronounced because the yard was flying in the logarithmic region and not in the viscous sub-layer.

3.4. Wake

In order to visualise the flow structures we used the second invariant of the velocity gradient, Q, which is a measure of the difference between the rotation rate and the shear rate of the flow. A high value of Q shows that flow rotation dominates the shear; therefore it can be interpreted as an index of the coherency of the flow structure (Hunt et al., 1988). Iso-surfaces of Q are coloured by the sign of the helicity, red being positive and blue negative. Helicity is computed with reference to the right-handed (positive) Cartesian coordinate system, where the x, y, and z axes are the longitudinal, transverse and vertical axes of the wind tunnel, positive towards the inlet, leeward and upwards, respectively.

Fig. 8 shows iso-surfaces of $Q=500\ s^{-2}$. On the left, the results for the 4M grid solved with a RANS approach are presented. The leeward side of the spinnaker is mostly covered by an iso-surface with negative helicity. The negative helicity is due to the negative spanwise vorticity of the boundary layer. Near the trailing edge, separation occurs leading to higher strain rate and lower Q. The tip vortex from the spinnaker's head is the largest visible flow structure. It convects along an axis, which is almost aligned with the wind direction. A similar vortex develops from the spinnaker's lower corner of the trailing edge and rotates in the opposite direction than the head vortex. Interestingly, the mid-span vortex is not visible, meaning that its coherency is weaker than those of the visualised structures.

In the centre of Fig. 8, the same grid is solved with a DES approach and the instantaneous flow field at 30 s is showed. Despite the low grid resolution (4M), LES allows solving these flow structures with a much greater extent than RANS. In particular, we found that the tip vortex generated from the head of the mainsail rolls around the spinnaker's tip vortex. Also, small flow structures, which become more visible with the 32M-grid DES (right in Fig. 8), appear near the sail foot. These are chordwise-stretched vortices generated from the spinnaker's foot and convected downstream intermittently, breaking down into smaller and smaller structures.

The limited RANS ability to model longitudinal vortices is partially due to the use of an isotropic linear turbulence model such as the Spalart–Allmaras, while further research should explore the use of anisotropic non-linear models in order to increase the production of longitudinal vorticity.

Spanwise-stretched vortices are generated from the trailing edge with a significantly lower frequency than those from the sail foot. The periods computed with the simulations did not allow an accurate measurement of these frequencies. Iso-surfaces of $Q=100\ s^{-2}$ show that these vortices do not break down as quickly as those from the foot but, conversely, are stretched between the tip vortex and the mid-span vortex. Fig. 9 shows the same comparison between different simulations as Fig. 8 but with a different perspective view and $Q=100\ s^{-2}$. In order to allow the spinnaker to be visible, the iso-surface of Q is hidden in a near-wall region. The mid-span vortex appears clearly in the two DES simulations, while it is hardly visible for the RANS simulation. In particular, with low grid resolution (centre in Fig. 9), the mid-span vortex appears as a continuous vortical tube, while its complicated structure is revealed using higher grid resolution.

Fig. 10 shows four views of iso-surfaces of $Q=100\ s^{-2}$ computed with the 32M-grid DES. In the four different views, only the flow structures upstream of sections A–D (Fig. 9) are shown. This sequence allows the visualisation of the correlation between the various flow structures in the sail wake. The vertically stretched trailing edge vortex rolls around the tip and the mid-span vortices, with both having horizontal axes and rotate clock-wise. Therefore,

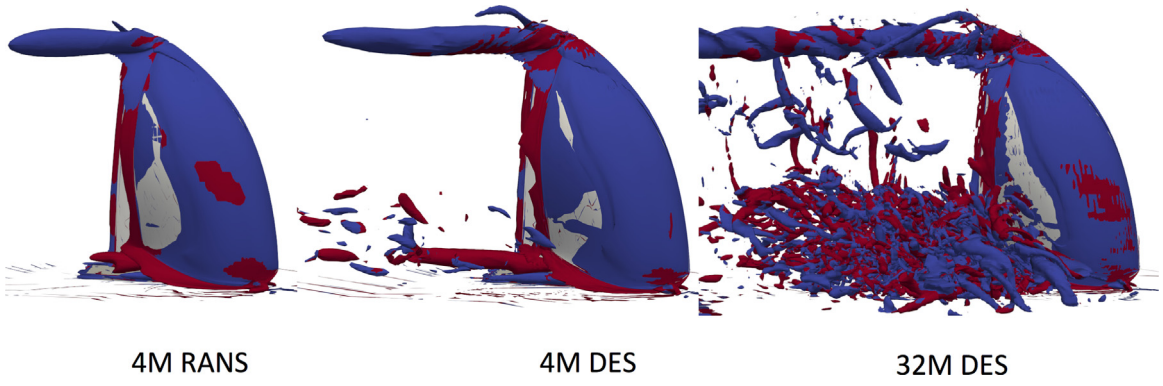

Fig. 8. Iso-surfaces of Q-criterion 500 s^{-2} coloured by helicity computed by RANS and DES with the 4M-cell and the 32M-cell grids. (For interpretation of the references to colour in this figure legend, the reader is referred to the web version of this article.)

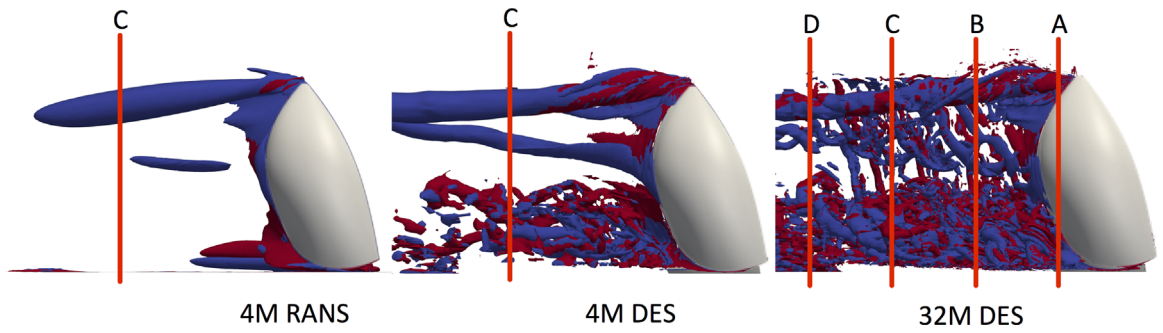

Fig. 9. Iso-surfaces of Q-criterion 100 s^{-2} coloured by helicity computed by RANS and DES with the 4M-cell and the 32M-cell grids. (For interpretation of the references to colour in this figure legend, the reader is referred to the web version of this article.)

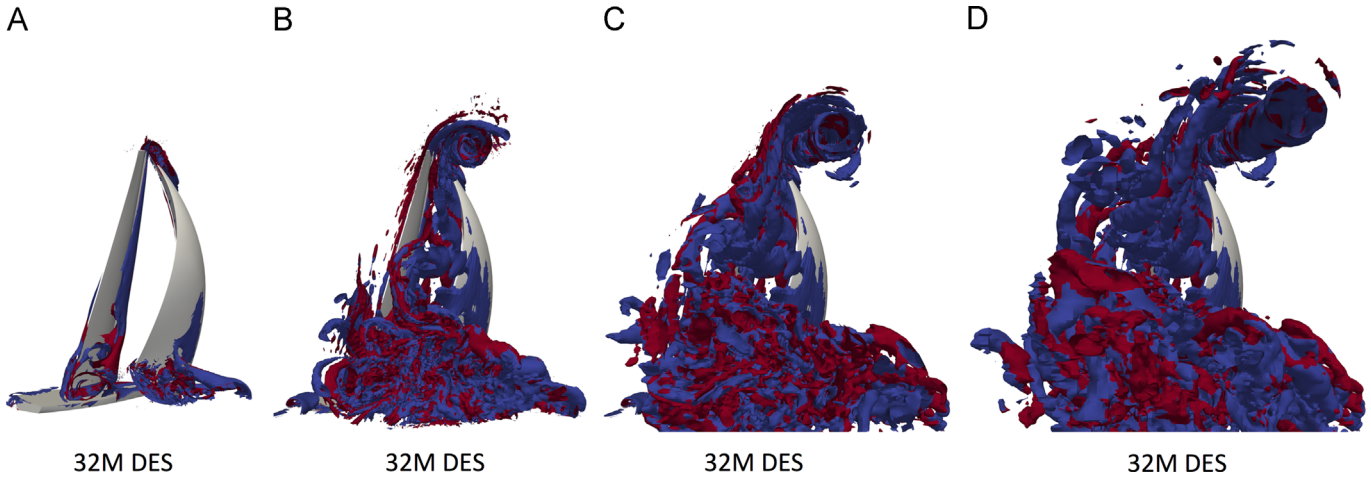

Fig. 10. Iso-surfaces of Q-criterion 100 s^{-2} coloured by helicity computed by DES with the 32M-cell grid viewed from four different positions downstream the yacht model. (For interpretation of the references to colour in this figure legend, the reader is referred to the web version of this article.)

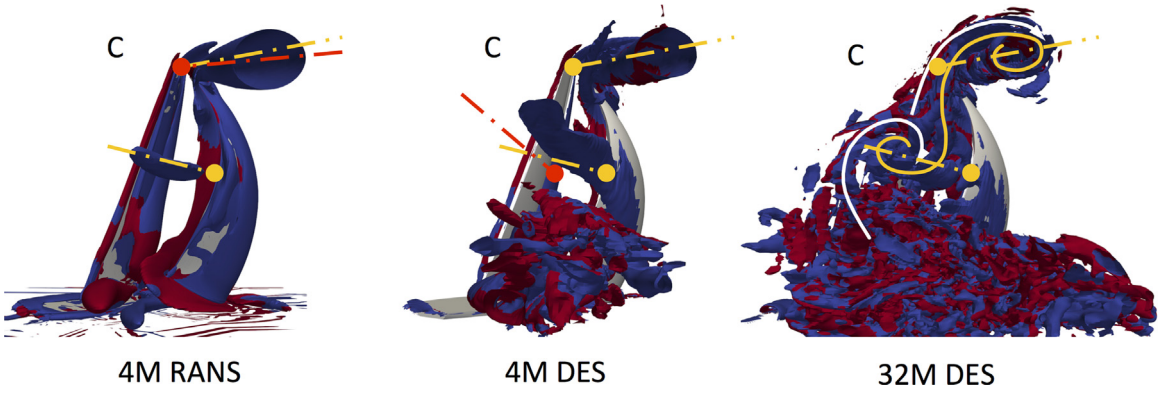

Fig. 11. Iso-surfaces of Q-criterion 100 s^{-2} coloured by helicity computed by RANS and DES with the 4M-cell and the 32M-cell grids viewed from position 'C'. (For interpretation of the references to colour in this figure legend, the reader is referred to the web version of this article.)

the trailing edge vortex, which is a tube parallel to the trailing edge when detached from the sail, assumes an 'S' shape while convecting downstream. The 'S' shape is schematically shown with a solid yellow line in Fig. 11 (right), while dotted lines show the two axes of the tip and mid-span vortices. The trailing edge vortex of the mainsail also rolls around the tip and mid-span vortices of the spinnaker, but due to its windward position, it is broken down into two vortices schematically showed by two white solid lines in Fig. 11 (right).

Fig. 11 shows the differences between 4M-RANS, 4M-DES and 32M-DES in modelling the evolution of the spinnaker and mainsail trailing edge vortices. In particular, the same view from section C in Fig. 10 is used in Fig. 11. The axes of the tip and mid-span vortices computed with high grid resolution are superimposed for comparison on the low grid-resolution RANS and DES, revealing that the lower grid resolution leads also to different directions of the axes. Videos of the simulations, which are available on the webpage of the first author (http://www.ignazioviola.com), show that the directions of these axes are stationary but different for the two DES simulations.

3.5. Forces

The forces measured with the two experiments showed significant differences and the numerical results of the different simulations are mostly in between the experimental ranges. Fig. 12 shows the computed and measured drag (C_D) and lift (C_L) coefficients defined as the total aerodynamic force acting on the sails, rigging and hull, divided by the far field dynamic pressure q_∞ and the sail surface.

For both C_D and C_L there are large differences between the coefficients measured with rigid and flexible sails, and those differences are larger than the differences between the various simulations. In particular, the experimental C_D ranges between 0.52 for the rigid sails and 0.64 for the flexible sails, while C_D computed with different DES simulations ranges between 0.52 and 0.56. Similarly, experimental C_L ranges between 1.31 for rigid sails and 1.51 for flexible sails, while C_L computed with different DES simulations ranges between 1.43 and 1.46.

C_D and C_L computed with RANS show the maximum differences with the experimental data. In particular, while C_D is between the maximum and minimum experimental C_D, C_L is 1% higher than the largest experimental C_L (flexible sails). C_D and C_L computed with DES are lower than those computed with RANS, though their trends are to increase with time and space resolution. However, different resolutions lead to small differences. In particular, differences are smaller than 1% and 3% for C_D and C_L, respectively. Interestingly, RANS and DES with the same grid resolution show larger differences than two DES simulations where the grid resolution is doubled.

Fig. 13 shows the breakdown of the aerodynamic coefficients for the spinnaker, the mainsail and the two sails combined but without hull and rigging. For the three cases, the coefficients were computed using only the sail area of the spinnaker, mainsail and the two sails together, respectively. These broken-down coefficients, which are

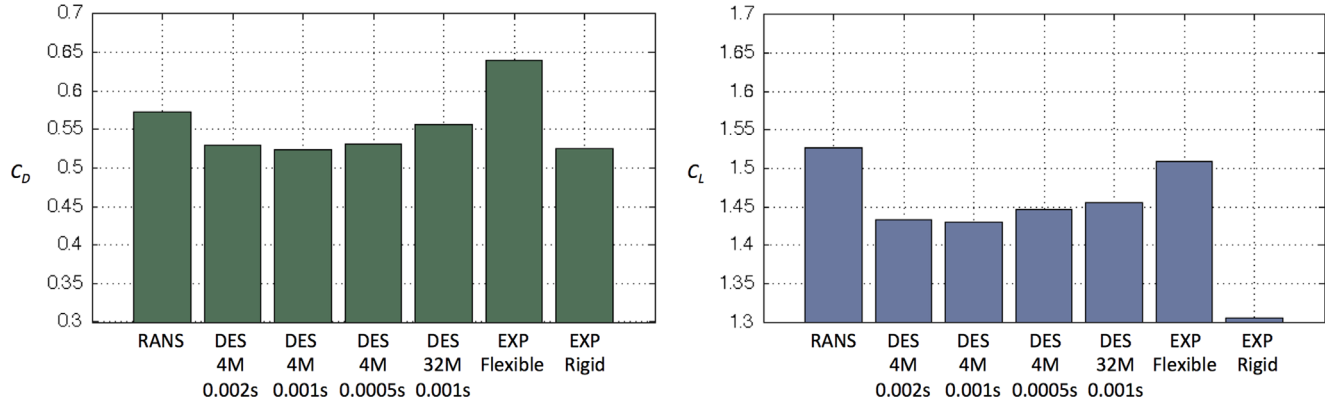

Fig. 12. C_D (left) and C_L (right) for the whole model computed with the numerical simulations and measured with the two experimental tests.

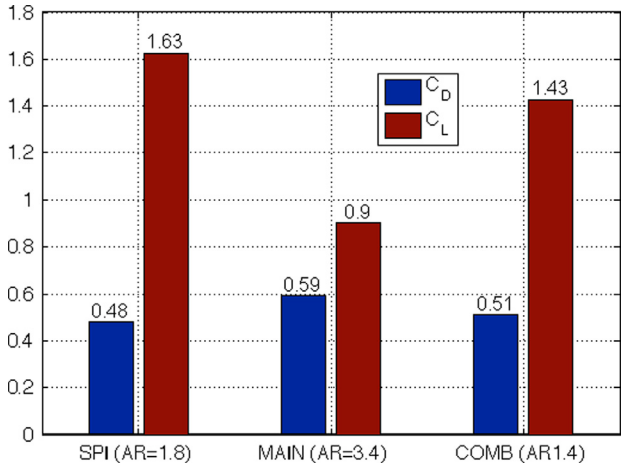

Fig. 13. C_D and C_L of the two sails computed by DES with the 32M-cell grid.

achieved with difficulty with experimental tests, show that the spinnaker is significantly more efficient than the mainsail, having higher C_L and lower C_D, despite its aspect ratio ($AR=1.8$) been about half the one of the mainsail ($AR=3.4$). This is largely due to the upwash and downwash experienced by spinnaker and mainsail, respectively.

3.6. Pressures

Fig. 14 shows the pressure distributions on five sail sections of the spinnaker: 7/8, 3/4, 1/2, 1/4 and 1/8 of the mitre respectively. C_p on both the windward and leeward pressure sides are presented versus the non-dimensional chordwise coordinate x/c. On the left in Fig. 14, C_p computed with RANS, 4M-DES and 32M-DES are presented. The two DES simulations are performed with a time step of 0.001 s. Also, C_p measured experimentally with both flexible and rigid sails are presented for comparison. Error bars are shown for the 32M-DES to highlight the regions where larger differences were found between the C_p computed with different grids and time steps. On the right in Fig. 14, C_p is computed with 4M-DES and three different time steps: 0.0005 s, 0.001 s and 0.002 s.

The sharp suction peak near the leading edge shows that the spinnaker operates very close to the ideal angle of attack, i.e. where the flow at the leading edge is parallel to the local sail surface leading to an attached boundary layer without formation of the LEV. At this limit condition, on the leeward side of the sail, the pressure decreases gradually from the leading edge to about the point of maximum sail curvature. The lowest sections of the spinnaker operate at angles of attack just above the ideal one, leading to a narrow LEV and to a high suction peak near the leading edge, while higher sections show a larger LEV.

The second suction peak at about 30% of the chord is due to the sail curvature. Downstream of the second peak, the adverse pressure gradient leads to trailing edge separation and thus to a pressure plateau.

From the lowest to the highest sections, the diameter of the LEV increases and therefore the first suction peak occurs more downstream. Also, the maximum camber of the sail and its associated second suction peak occur more downstream, and thus also trailing edge separation occurs more downstream.

On the highest section of the spinnaker, the LEV turns downstream and becomes the tip vortex (Figs. 7 and 8). Pressures on this section are measured almost along the vortex axis showing a slightly positive pressure gradient. In particular, a map of C_p on the sail surface (not shown in the present paper) reveals that the minimum pressure is along the LEV axis and between sections 3/4 and 1/8.

The larger differences between the numerical and experimental C_p are near the leading edge on the highest sections and near the trailing edge on the lowest sections. The differences on the 7/8 section are reflected on the 3/4 section and suggest that the highest sections were stalled in the experiment, leading to a flat base pressure instead of experiencing the suction due to the swirling flow. Differences are small on the lowest sections but the computed base pressure of the pressure plateau near the trailing edge is higher than the one measured experimentally, suggesting that trailing edge separation was under-predicted by the numerical simulations.

As a confirmation of the trends shown by the forces in Fig. 12, C_p computed with RANS and DES shows larger differences than C_p computed with different resolutions. Particularly, larger differences occur near the head and foot of the sail, while on the midsection of the spinnaker differences are smaller. On the lowest sections, RANS predicts a later trailing edge separation than DES and thus a larger suction peak correlated with the sail curvature. On the highest section the suction on the leeward side of the sail is quite sensitive to the different time steps tested with DES. Conversely, the same pressures are computed near the trailing edge and on the windward side of the sail when different grids and time resolutions are used.

4. Conclusions

In the present work, wind tunnel experiments on a 1:15th model-scale sailing yacht were modelled with Detached Eddy Simulations (DES). Several time and grid resolutions were tested in order to assess the numerical uncertainty. The experiments were also modelled with a Reynolds-averaged Navier–Stokes (RANS) approach for comparison

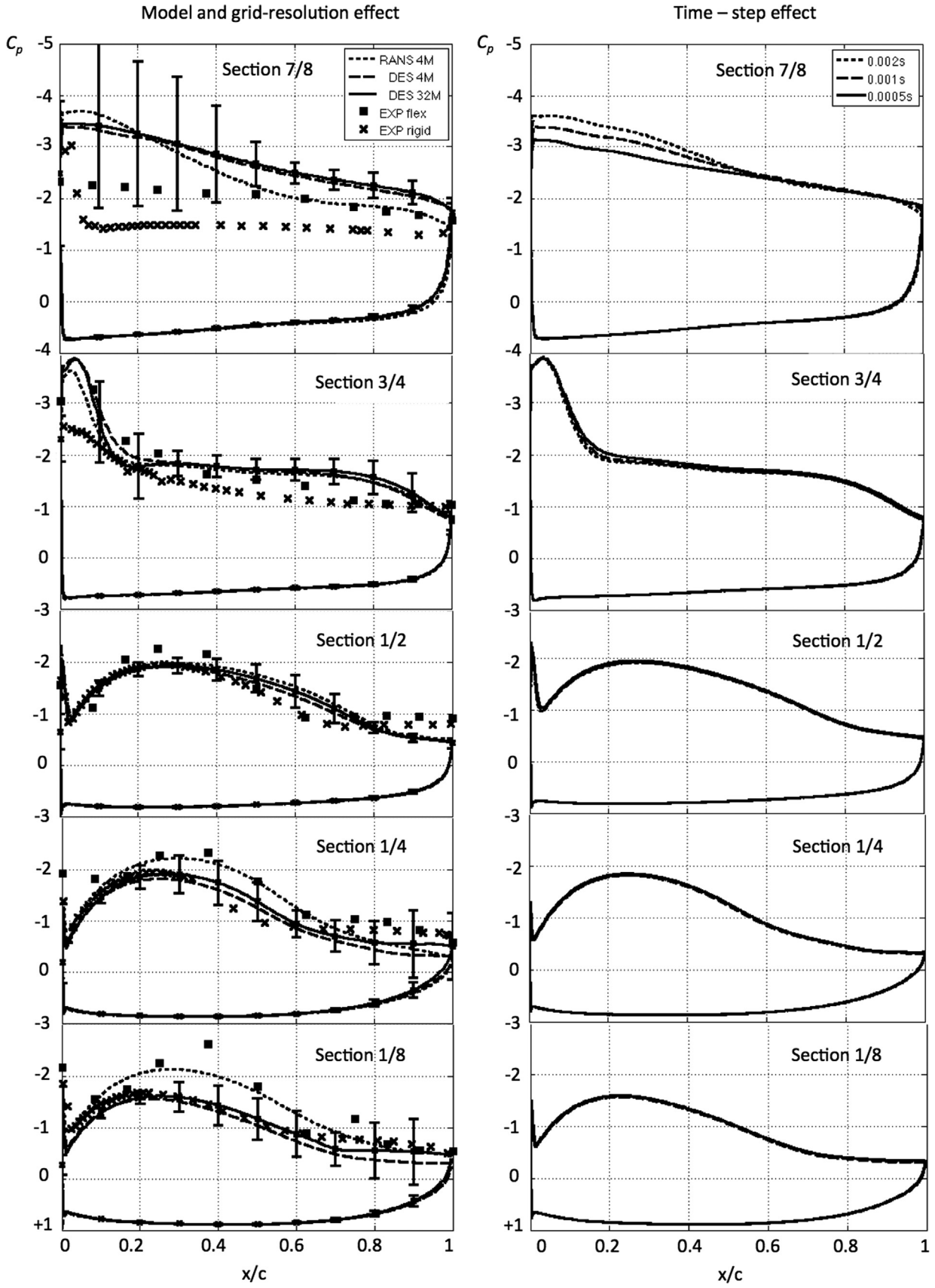

Fig. 14. C_p versus x/c on five horizontal sail sections computed with different simulations and measured with the two experimental tests.

with DES. The computed forces and surface pressure distributions were compared with those measured with both flexible and rigid sails in the wind tunnel.

An attached boundary layer was found on the windward side (pressure side) of the sails while the flow separates on the leeward side (suction side) along all the leading edge of the sails. Further

downstream the flow reattaches and a boundary layer grows along the chord until trailing edge separation occurs. On the spinnaker (foresail), the leading edge separation and reattachment form a coherent and steady leading edge vortex, which increases in diameter from the foot to the head, where it becomes the tip vortex and convects downstream in the direction of the far field velocity. The tip vortex from the head of the mainsail rolls around the one of the spinnaker.

The spanwise twist of the spinnaker leads to a mid-span helicoidal vortex with a horizontal axis and rotating in the same direction as the tip vortex. Its role on the aerodynamic performance of the sail is not clear and should be further explored. Vortical spanwise tubes are released from the trailing edges of the mainsail and the spinnaker and, while convecting downstream, these structures roll around the tip and mid-span vortices of the spinnaker. Vortical tubes are also detached intermittently from the sails' feet and these break down into smaller and smaller structures while convecting downstream.

Forces and pressures were almost independent from the time and space resolutions tested in the present work and showed similarities with those measured experimentally. The largest differences were observed on the suction side at the head of the spinnaker where the leading edge vortex turns into the tip vortex. Interestingly, the largest numerical–experimental differences and the largest differences between numerical simulations were found in the same regions, showing where the pressure fields are sensible to small changes of the Reynolds stresses.

DES allowed an improved understanding of the sails' wake topology compared to RANS. Importantly, it was found that the more resolved wake led to differences on the pressure distributions on the sails. Therefore it can be concluded that in order to accurately predict the aerodynamic forces in downwind conditions it is necessary to model with care the sails' wake. Based on this study, however, it is not possible to conclude that DES allows a more accurate solution than RANS. In fact, the two models were compared only with a coarse grid and with a linear isotropic turbulence model, which does not reflect the actual potential of the RANS approach. Also, the large discrepancies between experimental measurements and the lack of local flow measurements and turbulence data do not allow a proper validation of the numerical simulations.

Acknowledgements

This research was supported in part by CILEA Interuniversity Consortium (Italy), CFD Technologies (UK) and ANSYS (Italy), who kindly provided HPC resources, and licences of Pointwise and Fluent, respectively.

References

Birch, J.M., Dickinson, M.H., 2001. Spanwise flow and the attachment of the leading-edge vortex on insect wings. Nature 412, 729–733.

Bot, P., Viola, I.M., Flay, R.G.J., 2013. Wind-tunnel pressure measurements on model-scale rigid downwind sails. In: Proceedings of the 3rd International Conference on Innovations in High Performance Sailing Yachts. June 26th–29th, Lorient, France.

Braun, J.B., Imas, L., 2008. High fidelity CFD simulations in racing yacht aerodynamic analysis. In: Proceedings of the 3rd High Performance Yacht Design Conference. December 2nd–4th, Auckland, New Zealand.

Gursul, I., Wang, Z., Vardaki, E., 2007. Review of flow control mechanisms of leading-edge vortices. Prog. Aerosp. Sci. 43, 246–270.

Hedges, K.L., Richards, P.J., Mallison, G.D., 1996. Computer modelling of downwind sails. J. Wind Eng. Ind. Aerodyn. 63, 95–110.

Hunt, J.C.R., Wray, A.A., Moin, P., 1988. Eddies, stream, and convergence zones in turbulent flows. Studying Turbulence Using Numerical Simulation Databases, vol. 2 (no. 1); , pp. 193–208.

Maxworthy, T., 2007. The formation and the maintenance of a leading-edge vortex during the forward motion of an animal wing. J. Fluid Mech. 587, 471–475.

Miyata, H., Lee, Y.W., 1999. Application of CFD simulation to the design of sails. J. Mar. Sci. Technol. 4, 163–172.

Owen, P.R., Klanfer, L., 1953. On the Laminar Boundary Layer Separation From the Leading Edge of a Thin Airfoil. Defense Technical Information Center, pp. 220.

Paillaud, T., 2013. Pressure Distribution Measurements on a Rigid Asymmetric Spinnaker in a Wind Tunnel (M.Eng. thesis). Art et Metiers Paris Tech, 72pp.

Richards, P., Lasher, W., 2008. Wind tunnel and CFD modelling of pressures on downwind sails. In: Proceedings of the VI International Colloquium on Bluff Bodies Aerodynamics and Applications. July 20th–24th, Milan, Italy.

Smirnov, R., Shi, S., Celik, I., 2001. Random flow generation technique for large eddy simulations and particle dynamics modeling. J. Fluids Eng. 123 (2), 359–371.

Spalart, P.R., 2009. Detached eddy simulation. Annu. Rev. Fluid Mech. 41, 181–202.

Spalart, P.R., Deck, S., Shur, M.L., Squires, K.D., Strelets, M.K., Travin, A., 2006. A new version of detached-eddy simulation, resistant to ambiguous grid densities. Theor. Comput. Fluid Dyn. 20, 181–195.

Tabor, G.R., Baba-Ahmadi, M.H., 2010. Inlet conditions for large eddy simulation: a review. Comput. Fluids 39 (4), 553–567.

Videler, J.J., Stamhuis, E.J., Povel, G.D.E., 2004. Leading-edge vortex lifts swifts. Science 306, 1960–1962.

Viola, I.M., 2009. Downwind sail aerodynamics: a CFD investigation with high grid resolution. Ocean Eng. 36 (12–13), 974–984.

Viola, I.M., Flay, R.G.J., 2009. Force and pressure investigation of modern asymmetric spinnakers. Int. J. Small Craft Technol. 151 (B2), 31–40.

Viola, I.M., Flay, R.G.J., 2010. Pressure distribution on modern asymmetric spinnakers. Int. J. Small Craft Technol. 152 (B1), 41–50.

Viola, I.M., Flay, R.G.J., 2011. Sail pressures from full-scale, wind-tunnel and numerical investigations. Ocean Eng. 38, 1733–1743.

Viola, I.M., Bot, P., Riotte, M., 2013. On the uncertainty of CFD in sail aerodynamics. Int. J. Numer. Methods Fluids 72 (11), 1146–1164.

Wright, A.M., Claughton, A.R., Paton, J., Lewins, R., 2010. Off-wind sail performance prediction and optimisation. In: Proceedings of the 2nd International Conference on Innovations in High Performance Sailing Yachts. June 30th–July 1st, Lorient, France.